CO2 response screen in grass Brachypodium reveals the key role of a MAP kinase in CO2-triggered stomatal closure

Bryn N K Lopez, Paulo H O Ceciliato, Yohei Takahashi, Felipe J Rangel, Evana A Salem, Klara Kernig, Kelly Chow, Li Zhang, Morgana A Sidhom, Christian G Seitz, et al.

HAL Id: hal-04684743

https://hal.inrae.fr/hal-04684743v1

Submitted on 3 Sep 2024

Plant Physiology®

CO$_2$ response screen in grass *Brachypodium* reveals the key role of a MAP kinase in CO$_2$-triggered stomatal closure

Bryn N.K. Lopez,[1,†] Paulo H.O. Ceciliato,[1,*,†] Yohei Takahashi,[1,2] Felipe J. Rangel,[1] Evana A. Salem,[1] Klara Kernig,[1] Kelly Chow,[1]

Li Zhang,[1] Morgana A. Sidhom,[1] Christian G. Seitz,[3,‡] Tingwen Zheng,[1] Richard Sibout,[4]

Debbie L. Laudencia-Chingcuanco,[5] Daniel P. Woods,[6] James Andrew McCammon,[3] John P. Vogel,[7] and Julian I. Schroeder[1,*]

[1]School of Biological Sciences, Cell and Developmental Biology Department, University of California San Diego, La Jolla, CA 92093-0116, USA
[2]Institute of Transformative Bio-Molecules (ITbM), Nagoya University, Nagoya, Aichi 464-0813, Japan
[3]Department of Chemistry and Biochemistry, University of California San Diego, La Jolla, CA 92093, USA
[4]Biopolymères Interactions Assemblages, Equipe Paroi Végétale et Polymères Pariétaux (PVPP), Impasse Y. Cauchois/Site de la Géraudière BP71627, Nantes 44316 cedex 03, France
[5]Crop Improvement and Genetics Research, USDA, ARS, PWA, WRRC-CIG, Albany, CA 94710, USA
[6]Department of Plant Sciences, University of California, Davis, CA 95616, USA
[7]U.S. Department of Energy Joint Genome Institute, Lawrence Berkeley National Laboratory, Berkeley, CA 94720, USA
*Author for correspondence: jischroeder@ucsd.edu (J.I.S.), paulo.ceciliato@gmail.com (P.H.O.C.)
[†]These authors contributed equally.
[‡]Present address: Department of Computer Science, University of Chicago, Chicago, Illinois, and Data Science and Learning Division, Argonne National Laboratory, Chicago, Illinois.
The author responsible for distribution of materials integral to the findings presented in this article in accordance with the policy described in the Instructions for Authors (https://academic.oup.com/plphys/pages/General-Instructions) is Julian Schroeder (jischroeder@ucsd.edu).

Abstract

Plants respond to increased CO$_2$ concentrations through stomatal closure, which can contribute to increased water use efficiency. Grasses display faster stomatal responses than eudicots due to dumbbell-shaped guard cells flanked by subsidiary cells working in opposition. However, forward genetic screening for stomatal CO$_2$ signal transduction mutants in grasses has yet to be reported. The grass model *Brachypodium distachyon* is closely related to agronomically important cereal crops, sharing largely collinear genomes. To gain insights into CO$_2$ control mechanisms of stomatal movements in grasses, we developed an unbiased forward genetic screen with an EMS-mutagenized *B. distachyon* M5 generation population using infrared imaging to identify plants with altered leaf temperatures at elevated CO$_2$. Among isolated mutants, a "*chill1*" mutant exhibited cooler leaf temperatures than wild-type Bd21-3 parent control plants after exposure to increased CO$_2$. *chill1* plants showed strongly impaired high CO$_2$-induced stomatal closure despite retaining a robust abscisic acid-induced stomatal closing response. Through bulked segregant whole-genome sequencing analyses followed by analyses of further backcrossed F4 generation plants and generation and characterization of sodium azide and CRISPR-cas9 mutants, *chill1* was mapped to a protein kinase, *Mitogen-Activated Protein Kinase 5* (*BdMPK5*). The *chill1* mutation impaired BdMPK5 protein-mediated CO$_2$/HCO$_3^-$ sensing together with the High Temperature 1 (HT1) Raf-like kinase in vitro. Furthermore, AlphaFold2-directed structural modeling predicted that the identified BdMPK5-D90N *chill1* mutant residue is located at the interface of BdMPK5 with the BdHT1 Raf-like kinase. BdMPK5 is a key signaling component that mediates CO$_2$-induced stomatal movements and is proposed to function as a component of the primary CO$_2$ sensor in grasses.

Introduction

The atmospheric CO$_2$ concentration has continuously increased since the industrial revolution and has long since surpassed the highest levels recorded in human history and is continuing to rise at a high rate (NASA, 2022; Stocker et al. 2013). The rise in CO$_2$ levels will have a profound impact on the growth and development of plants, including crops. Some models predict a net increase in plant growth worldwide due to effects of CO$_2$ fertilization under well-watered conditions (Zhu et al. 2016). However, crop productivity is negatively impacted by rising CO$_2$ concentrations as it increases the risk of frequency, duration, and intensity of heat waves due to the heat-trapping nature of greenhouse emissions (Wahid et al. 2007; Asseng et al. 2015; Zheng et al. 2019). Drought stress is expected to increase in both occurrence and severity in response to climate change (Hetherington and Woodward 2003; Sherrard and Maherali 2006). Abiotic stressors such as salinity and drought are estimated to contribute to major agricultural yield losses globally (Hetherington and Woodward 2003; Stocker et al. 2013; Zhu et al. 2016). These circumstances highlight the need for an increased understanding of how water use efficiency (WUE) of important cereal crops is regulated.

Stomatal pores adjust in response to environmental conditions to regulate CO$_2$ uptake and water loss. CO$_2$-induced reduction in stomatal apertures can contribute to an increase in WUE in grasses by limiting transpiration while maintaining CO$_2$ assimilation (De Souza et al. 2008; Allen et al. 2011; Wang et al. 2015). Stomata are present on leaf surfaces and facilitate gas exchange in response to diverse stimuli (Hetherington and Woodward 2003; Bertolino et al. 2019). Stomata are composed of a pair of

guard cells regulating stomatal movements by adjusting relative turgor pressure of the guard cells (Raschke and Fellows 1971; Willmer and Fricker 1996; MacRobbie 2000). Turgor pressure is mediated by water and ion movement across guard cell membranes (Raschke 1975; MacRobbie 2006). When exposed to high CO_2 levels, stomatal pores close, leading to a reduced stomatal conductance and limited evapotranspiration, resulting in an increase in canopy leaf temperature (Hauser et al. 2019; Harrison et al. 2020; Merlot et al. 2002, Mustilli et al. 2002; Hetherington and Woodward 2003; Xie et al. 2006).

In darkness, respiration causes an increase in leaf CO_2 concentrations, which leads to stomatal closure in C3 and C4 plants (Zhang et al 2018). Stomatal closure induced by elevated CO_2 levels is initiated as CO_2 enters guard cells and carbonic anhydrases catalyze the equilibration to protons and HCO_3^- (bicarbonate) (Hu et al. 2010; Hu et al. 2015; Wang et al. 2015; Chen et al. 2017; Kolbe et al. 2018; Zhang et al. 2018). MAP kinases have been shown to play an important role in CO_2-induced stomatal closing in eudicots (Marten et al. 2008; Jakobson et al. 2016; Tõldsepp et al. 2018; Takahashi et al. 2022). Increased CO_2 is detected by Mitogen-Activated Protein Kinase 4 and 12 (MPK4/12) together with the High Temperature 1 (HT1) Raf-like protein kinase which in combination serve as a primary stomatal CO_2 sensor in Arabidopsis (*Arabidopsis thaliana*) (Takahashi et al. 2022). High CO_2/bicarbonate-induced interaction of MPK4/12 with HT1 causes inhibition of the HT1 protein kinase activity, preventing downstream activation of the Convergence of Blue Light and CO_2 (CBC1/CBC2) protein kinases (Takahashi et al. 2022). Thus, high CO_2 is modeled to prevent CBC1/CBC2 and HT1 from inhibiting S-type anion channels, which contribute to stomatal closure (Hiyama et al. 2017, Takahashi et al. 2022). Conversely, active HT1 protein kinase leads to downstream activation of the CBC1 protein kinase, which leads to initiation of stomatal opening mechanisms (Hiyama et al. 2017).

Monocots possess stomata composed of dumbbell-shaped guard cells flanked by functional subsidiary cells unlike the kidney-shaped guard cells found in eudicots. This difference allows for the faster stomatal responses observed in monocots when exposed to stimuli (Raschke and Fellows 1971; Hetherington and Woodward 2003; Fahad et al. 2017; Raissig et al. 2017; Lawson and Vialet-Chabrand 2019). However, unbiased forward genetic screens for stomatal movements have been difficult to perform in grasses including cereal crops, and to date, no forward genetic screens have been reported on the stomatal CO_2 responses in grasses.

Brachypodium (*Brachypodium distachyon*) is emerging as a model organism for monocots as opposed to the widely investigated eudicot model *A. thaliana*, which has been shown to have very limited genomic collinearity to staple cereal crops (Keller and Feuillet 2000; Vogel and Bragg. 2009; Brkljacic et al. 2011; Scholthof et al. 2018). In contrast to Arabidopsis, Brachypodium is much more closely related to cereal crops with a high degree of evolutionary collinearity (Scholthof et al. 2018). *B. distachyon* compared with other monocotyledonous models has a smaller size, compact genome, and short lifespan; making it favorable for high-throughput screening (Brkljacic et al. 2011; Scholthof et al. 2018; Raissig and Woods 2022).

In the present study, we screened over 1,000 M5 generation EMS-mutagenized *B. distachyon* lines for impairments in the stomatal CO_2 response. We report isolation of a mutant, *chill1*, that strongly impairs high CO_2-induced stomatal closure and show that this mutant on average has a higher stomatal conductance and a disrupted response to increased CO_2 while retaining robust abscisic acid (ABA)-induced stomatal closing. Genetic, physiological, biochemical, and structural modeling analyses suggest that *chill1* encodes a central component of CO_2 regulation of stomatal movements in grasses.

Results

Stomatal CO_2 response screen in *B. distachyon* identifies *chill* mutants

Rapid stomatal closure is induced by exposure to elevated CO_2, reducing stomatal conductance and evapotranspiration. This in turn causes higher leaf temperatures which can be measured through infrared imaging (Mustilli et al. 2002; Xie et al. 2006; Hauser et al. 2019). The use of infrared imaging has been shown to be a reliable high-throughput method for screening for mutants involved in stomatal movements such as *ost1* (Mustilli et al. 2002; Xie et al. 2006). We first determined whether mature *B. distachyon* plants show a measurable temperature response to CO_2 by infrared imaging. Side views of plant canopies in this grass showed robust temperature changes in response to ambient CO_2 concentration changes (Supplementary Fig. S1). Based on these pilot experiments, a high-throughput forward genetic infrared imaging screen was pursued with a population of >1,000 individually stored EMS-mutagenized M5 generation Brachypodium lines to screen for plants with reduced sensitivity to elevated CO_2 by selecting plants appearing cooler than the wild-type (WT) control (Bd21-3).

Through this high-throughput forward genetic infrared leaf imaging screen conducted at high CO_2 concentrations (~900 ppm) of 5 plants each of 1,075 individually stored M5 generation EMS-mutagenized *B. distachyon* pools, we isolated 50 putative "*chill*" mutants with leaf temperatures cooler than the WT parent (Bd21-3). In a secondary screen, after rescreening 5 plants from each of the individually stored M5 seed stock, 28 of the 50 putative mutants showed cool leaves at elevated CO_2 (900 ppm). In a tertiary screen in the following (M6) generation, 7 of the 28 mutants could not be confirmed as markedly different from WT controls through infrared imaging analyses and were removed as candidates. The remaining 21 mutants were reconfirmed by rescreening in the M6 generation and named *chill* mutants.

Chill1 shows greatly impaired CO_2 response, but functional ABA response

Of the mutants identified in this screen, we initially focused on a mutant that we have named *chill1* (Fig. 1A), which showed cooler leaf temperatures than WT (Bd21-3) controls in infrared imaging following exposure to increased CO_2 (900 ppm) (Fig. 1A). Infrared imaging following exposure to low CO_2 (150 ppm) was also pursued initially; however, clear differences could not be observed between mutant and WT (Bd 21-3). Furthermore, there was some experiment-to-experiment biological variation in growth of *chill1* vs. Bd21-3 parent control plants. However, no consistent trend was observed for this difference in overall plant size between mutant and the parental Bd21-3 control. To determine whether the difference observed in canopy leaf temperature was related to stomatal development or stomatal movements, stomatal index and density analyses were conducted comparing *chill1* with the parental WT control (Bd21-3). No significant difference could be observed in stomatal index and density (Fig. 1, B and C).

Stomatal conductance analyses were pursued. Consistent with the observation of similar leaf temperatures at low (150 ppm CO_2)
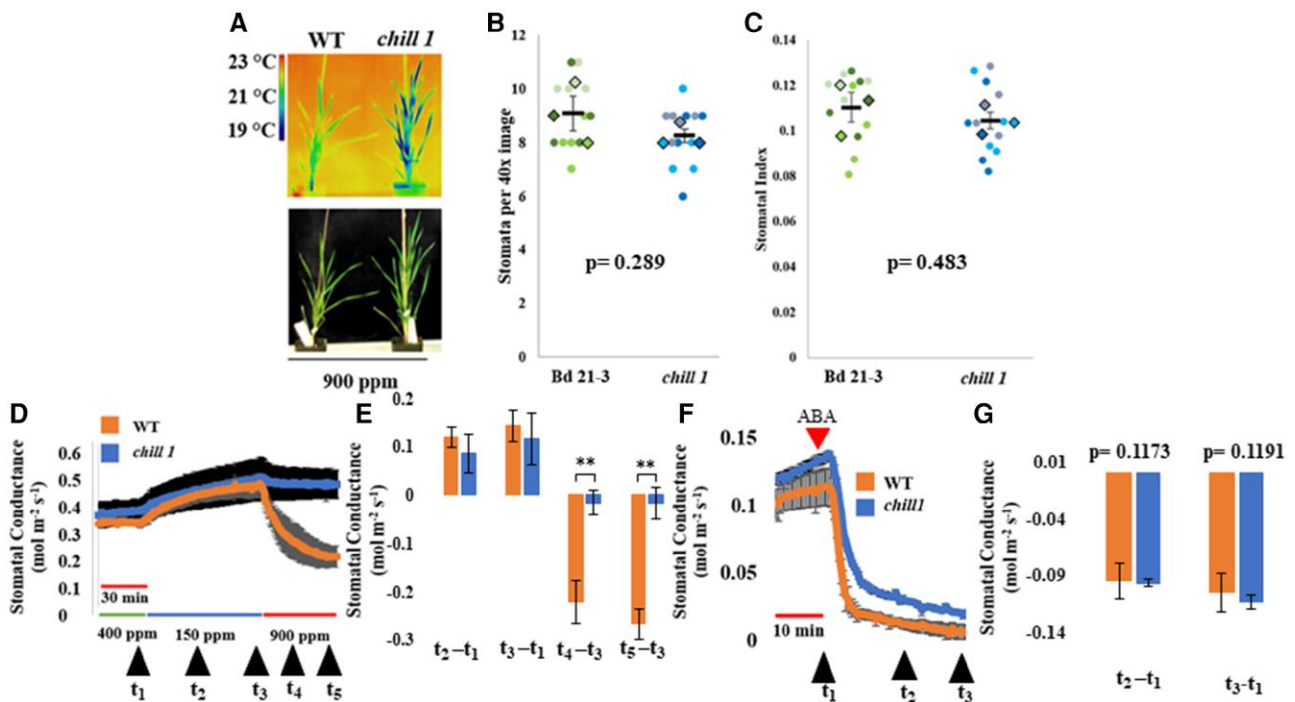
Figure 1. *Chill 1* mutant shows impaired stomatal response to changes in CO$_2$ but remains responsive to exogenous ABA. **A)** Four- to 5-wk-old *B. distachyon* plants were imaged following exposure to high CO$_2$. Pseudo-colored temperature scale is on the left ($^{\circ}$C). (top infrared image, bottom photo of the same plants). **B)** Stomatal density and **C)** stomatal index were determined using leaf imprints created of the 4th true leaf of plants with 3 independent replicates plants per genotype with 4 images per plant. Circles represent counts per each image, while diamonds are the average per each plant. Error bars represent SEM, while *P*-values were obtained from 2-tailed *t* tests comparing mutant with WT. Independent biological replicates per genotype were $n = 3 \pm$ SEM. ANOVA results with post hoc Tukey tests for **B)** stomatal density between groups are $P = 0.298$. ANOVA results for **C)** stomatal index between groups is $P = 0.4831$. Post hoc Tukey test for both index and density determined there was no significant differences between groups. **D)** Stomatal conductance was quantified using a gas exchange analyzer. Data shown are the average of $n = 3$ plants per genotype $\pm$ SEM using 4 leaves per plant. **E)** Change in amplitude over time from data as in in panel **D)** ($n = 3$ replicates per genotype $\pm$ SEM). Colors correspond to panel **D)** where WT is orange and *chill1* is blue. Statistical differences were determined by a 1-way ANOVA with post hoc Tukey test for $n = 3$ replicates per genotype. *P*-values for changes over time are as follows: $t_2 - t_1$ *P*-value $= 0.511$, $t_3 - t_1$ *P*-value $= 0.704$, $t_4 - t_3$ *P*-value $= 0.016$, and $t_5 - t_3$ *P*-value $= 0.005$. *******P*-value of <0.01. **F)** Stomatal conductance was recorded prior to and following addition of 2 μM ABA. Data shown are the average of $n = 3 \pm$ SEM plants per genotype using 1 leaf per experiment and genotype. **G)** Stomatal conductance changes $\pm$ SEM as calculated for the illustrated time points as in panel **F)** for $n = 3$ replicates per genotype. Colors correspond to panel **F)** where orange is WT and *chill1* is blue. One-way ANOVA with post hoc Tukey test values are shown. **P*-value < 0.05, *******P*-value of <0.01.

between *chill1* and the WT parent Bd21-3 control, stomatal conductance was comparable at low CO$_2$ (Fig. 1, D and E). Interestingly, *chill1* plants showed a dramatically reduced response to elevated CO$_2$ when compared with WT controls (Fig. 1, D and E). We next investigated stomatal closure in response to ABA. Notably, *chill1* leaves responded similarly to WT following the addition of 2 μM ABA to the transpiration stream of 5-wk-old leaves (Fig. 1, F and G).

Determination of inheritance patterning

To determine inheritance patterns, *chill1* plants were backcrossed to the parental strain Bd21-3 (see Materials and methods). The F1 *chill1* × Bd21-3 population was initially analyzed by infrared imaging experiments following exposure to increased (1,000 ppm) CO$_2$. F1 crossed *chill1* × Bd21-3 plants exhibited a phenotype more similar to that of WT (Bd21-3 controls) (Fig. 2A). These data were consistent across 4 individual *chill1* × Bd21-3 F1 plants. F1 plants were also analyzed in stomatal conductance analyses to quantify real-time responses to shifts in CO$_2$ concentrations. The F1 backcrossed plants exhibited a robust response to high CO$_2$ (900 ppm) consistently across 3 biological replicates (Fig. 2, B and C).

Selection of F2 plants and bulked segregant analyses

Tillers were created from these F1 plants (Woods and Amasino 2015; O'Connor et al. 2017) to generate large numbers of seeds for an F2 mapping population (Supplementary Fig. S2). The 4-wk-old F2 mapping population of ~560 individual F2 plants was screened following 1,000 ppm CO$_2$ exposure. Screening was done with 2 to 4 F2 plants alongside a parallel-grown WT plant (Bd21-3) as a control for all plants that were screened (Fig. 3). In an initial analysis of all infrared images of F2 plants, 116 of ~560 plants screened showed a *chill1*-like phenotype (21%). Analyses of F1 and F2 generations indicated that the *chill1* phenotype is due to a single locus recessive mutation. All images were also independently reanalyzed by 3 laboratory members in a very conservative manner to reduce false positive selection for whole-genome sequencing (WGS)-based bulked segregant mapping analyses (BSA). Of the plants screened, 57 plants (10%) were individually selected by all members as clearly showing a *chill1*-like phenotype and 50 plants (9%) were selected to be strongly WT-like to be used as a point of comparison in BSA experiments. The 57 plants selected as *chill1*-like were named mutant pool (M-pool) and were screened a second time for those which exhibited the strongest phenotype. A smaller mutant pool
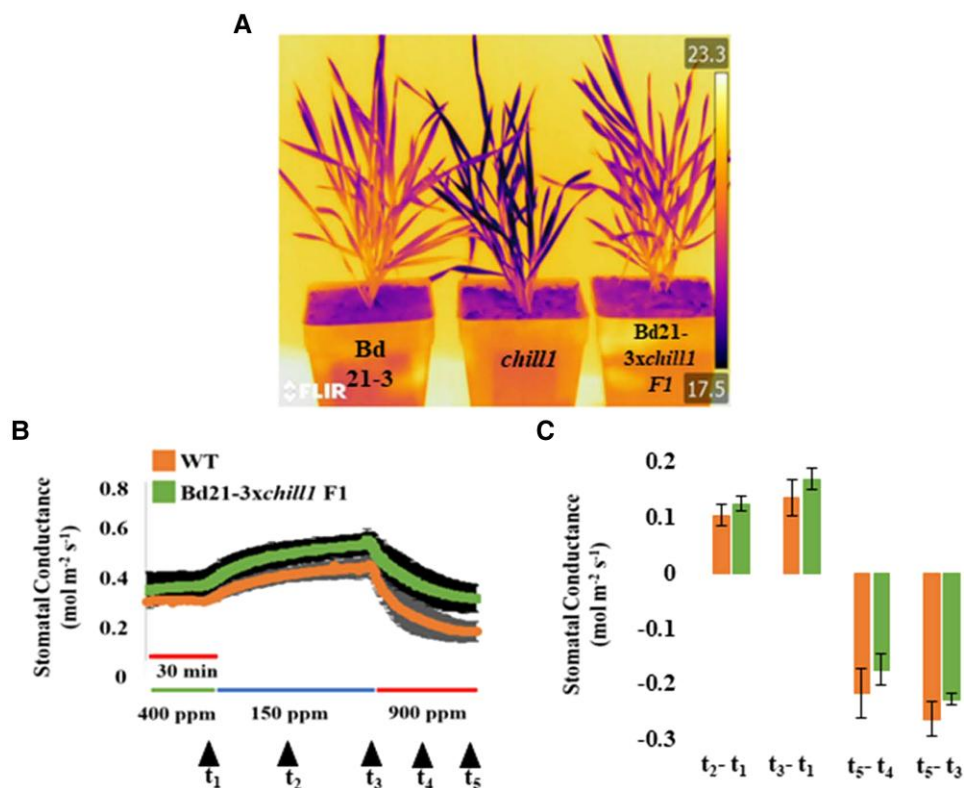
Figure 2. Characterization of *chill1* F1 backcross. **A)** Five- to 6-wk-old backcrossed *chill1 B. distachyon* plants were analyzed (right) by infrared imaging following 2 h exposure to 1,000 ppm CO_2 alongside parental WT control Bd 21-3 (WT) and the *chill1* mutant. Pseudo-colored temperature scale is on the right (°C). **B)** Stomatal conductance response of the F1 cross of the parent line Bd21-3 with the *chill1* mutant was analyzed using a gas exchange analyzer. Data shown are the average of $n = 3 \pm$ SEM experiments using 4 leaves per genotype in each experiment. **C)** Stomatal conductance changes $\pm$ SEM as calculated for the illustrated time points from panel **B)** with $n = 3$ replicates per genotype. Colors correspond to legend presented in panel **B)** wherein WT is orange and the F1 cross is green. One-way ANOVA with post hoc Tukey test are shown. *P*-values for changes over time are as follows: $t_2 - t_1$ *P*-value is $P = 0.4154$, $t_3 - t_1$ *P*-value is 0.4260, $t_4 - t_3$ *P*-value is 0.4796, and $t_5 - t_3$ *P*-value is 0.3432.
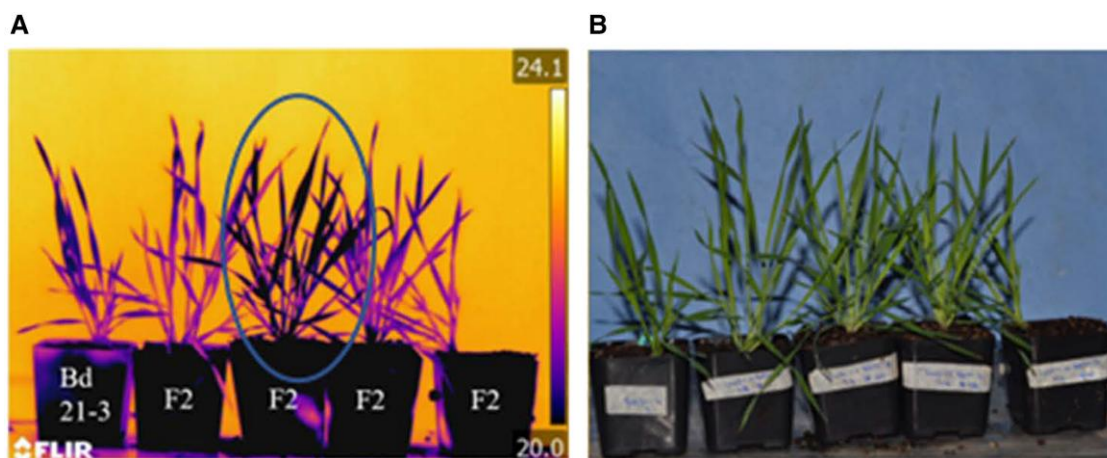

Figure 3. *Chill1* × Bd21-3 parent F2 infrared imaging selection. **A)** Four- to 5-wk-old *chill1* × Bd 21-3 F2 backcrossed plants were exposed to 1,000 ppm CO_2 for 2 h then immediately imaged using an infrared imaging camera. The left most plant is the Bd21-3 parent line (WT). The blue ellipse highlights a plant showing a *chill1-like* lower temperature. Pseudo-colored temperature scale is on the right (°C). **B)** Color images were taken at the same time for plant/leaf identification.

of 25 individuals with the strongest *chill* leaf canopy phenotype was named strongest mutant pool (SM-pool).

DNA from F2 plants selected as *chill1*-like or WT-like was pooled and submitted for WGS to be utilized in BSA (Michelmore et al 1991). Quality checks were performed on sequence reads before use in further analyses (Supplementary Fig. S3). QTLseqr (Mansfeld and Grumet 2018) was used to analyze files and generate visual representations of the −log$_{10}$-(*P*-value) derived from G' values (Magwene et al 2011) (Fig. 4), which are generated based on SNPs called during analysis (Takagi et al. 2013) (see Materials and methods). BSA analyses of both the M-pool and the SM-pool showed likely heterozygous
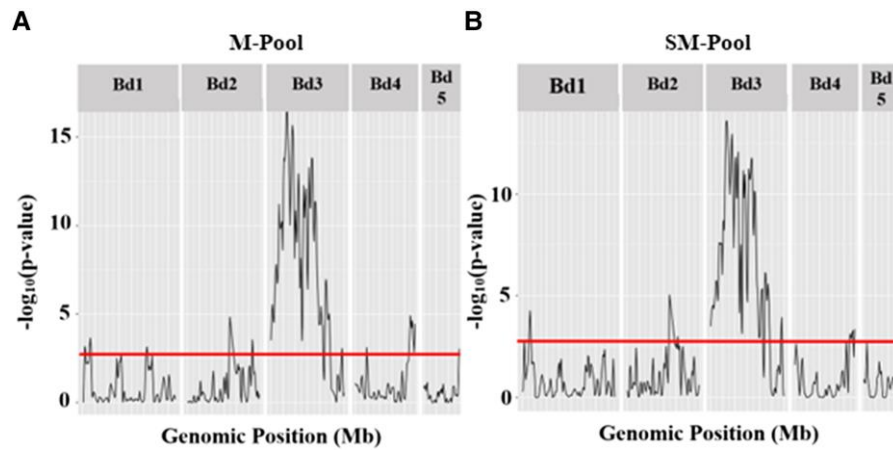
Figure 4. QTLseqr output for BSA for M- and SM-pool, respectively. BSA was performed with 2 different data sets. The (left) M-pool (57 *chill1*-like individuals) was used as the mutant pool, and (right) the SM-pool (37 *chill1*-like individuals with the most robust infrared image phenotypes) was used as the small mutant pool. In both analyses, the WT-like pool (50 WT-like F2 individuals) was used as the reference. The *x* axis shows the chromosome number and genomic position. The *y* axis represents the −log10(*P*-value) derived from the G' value (see Materials and methods). The genome-wide false discovery rate of 0.01 is indicated by the red line.

and homozygous variants on chromosome 3 (Bd3) with some smaller potential peaks on other chromosomes (Fig. 4). Most of the called variants were heterozygous. We filtered the variant data for homozygous variants and compared the called variants in the M-pool and SM-pool vs. the WT-like pool. Called homozygous variants from pooled short read whole-genome sequences in both the M-pool and SM-pool were analyzed for variants predicted to cause impactful mutations and were compiled into a single list via SnpEff and QTLseqR (Cingolani et al. 2012; Mansfeld and Grumet 2018). Heterozygous variants were excluded from further analyses on the basis that *chill1* behaves like a recessive mutant as determined by the F1 generation phenotype and F2 generation segregation. After variants were filtered for homozygosity, 4 variants were called for the M-pool and 3 for the SM-pool. Variants in 2 genes (BdiBd21-3.3G0222500 and BdiBd21-3.3G0296900) were called in both pools leading to a total compiled list of 5 potential candidate genes (Fig. 5A).

To reduce the number of potential candidate variant genes, additional *chill1* F2 plants were screened and those selected as cooler than WT controls were backcrossed to the WT parent line Bd21-3 a second time. Plants were taken into the F4 generation and were rescreened by infrared imaging. DNA was extracted from those plants selected individually by 2 different laboratory members to be cooler than WT (Bd21-3) controls. DNA from selected F4 plants was used to confirm the presence of called variants via Sanger sequencing. Of the remaining 5 candidate genes, 4 were excluded from further analyses based on the absence of the called variant or heterozygosity at the called loci, as determined by Sanger sequencing (Fig. 5A). The only candidate which could not be excluded was in the BdiBd21-3.3G0222500 gene. The called variant in exon 2 was confirmed by Sanger sequencing and found to be homozygous in 11 individually analyzed *chill1*-like F4 plants but was not found in 3 WT (Bd21-3) controls nor in a F4 plant selected as WT-like (Fig. 5B). These analyses suggested that the variant in BdiBd21-3.3G0222500 may be responsible for the *chill1* phenotype. Interestingly, phylogenetic analyses show that BdiBd21-3.3G0222500 encodes a protein with a high protein sequence similarity to both *Arabidopsis AtMPK4* and *AtMPK12* (Supplementary Fig. S4).

Sequence-indexed Na$^+$ azide lines and CRISPR mutagenesis identify *chill1*

To further test the hypothesis that the variant in BdiBd21-3.3G0222500 may be responsible for the *chill1* phenotype, we searched the Phytozome (phytozome-next.jgi.doe.gov) database for sequence-indexed sodium azide (NaN)-mutagenized lines (Dalmais et al 2013) predicted to contain a mutation in BdiBd21-3.3G0222500. The NaN0770 line was obtained and was sequenced to confirm the presence of the predicted exonic T to C point mutation sustained at position 14,916,843 on chromosome Bd3 via Sanger sequencing. NaN0770 plants in which the predicted mutation was confirmed to be homozygous were analyzed by infrared imaging alongside the original *chill1* mutant allele, WT controls, and F1 crossed plants of the NaN0770 line and WT Bd 21-3 plants (Fig. 6, A and B). Infrared imaging of the NaN0770 line showed leaf canopy temperatures that were intermediate to the *chill1* and WT phenoptypes or more similar to *chill1* than to WT control plants (Fig. 6A). In contrast, NaN0770×WT F1 backcrossed plants appeared more similar to WT controls (Fig. 6A). NaN0770 was also analyzed in an allelism test by crossing with *chill1*, wherein the F1 cross plants appeared cooler than WT (Fig. 6, C and D). Canopy temperatures in the NaN0770 line and in the F1 cross to *chill1* were cooler than WT (Bd 21-3) controls but less pronounced than *chill1*. These data indicated that the NaN0770 line has a less severe mutant phenotype compared with *chill1* (Fig. 6, C and D).

Taken together, the above data provide evidence that the *chill1* variant in BdiBd21-3.3G0222500 may be responsible for the cool leaf canopy temperature. To further test this hypothesis, CRISPR-cas9 lines were generated using a guide RNA (gRNA) targeting BdiBd21-3.3G0222500, which lies in a gene annotated as *Mitogen-Activated Protein Kinase 5* (*BdMPK5*) (Fig. 7A). *BdMPK5* was amplified in both WT and CRISPR-cas9 lines and aligned for comparison to determine the presence of mutations sustained within the gene of interest leading to identification of individual CRISPR alleles in *BdiBd21-3.3G0222500*. Individual T2 generation CRISPR plants were also genotyped to detect the presence or absence of cas9. T2 CRISPR plants were additionally genotyped to confirm mutations sustained within *BdMPK5*. Only plants which were confirmed to be cas9-free (Supplementary Fig. S5) and to have
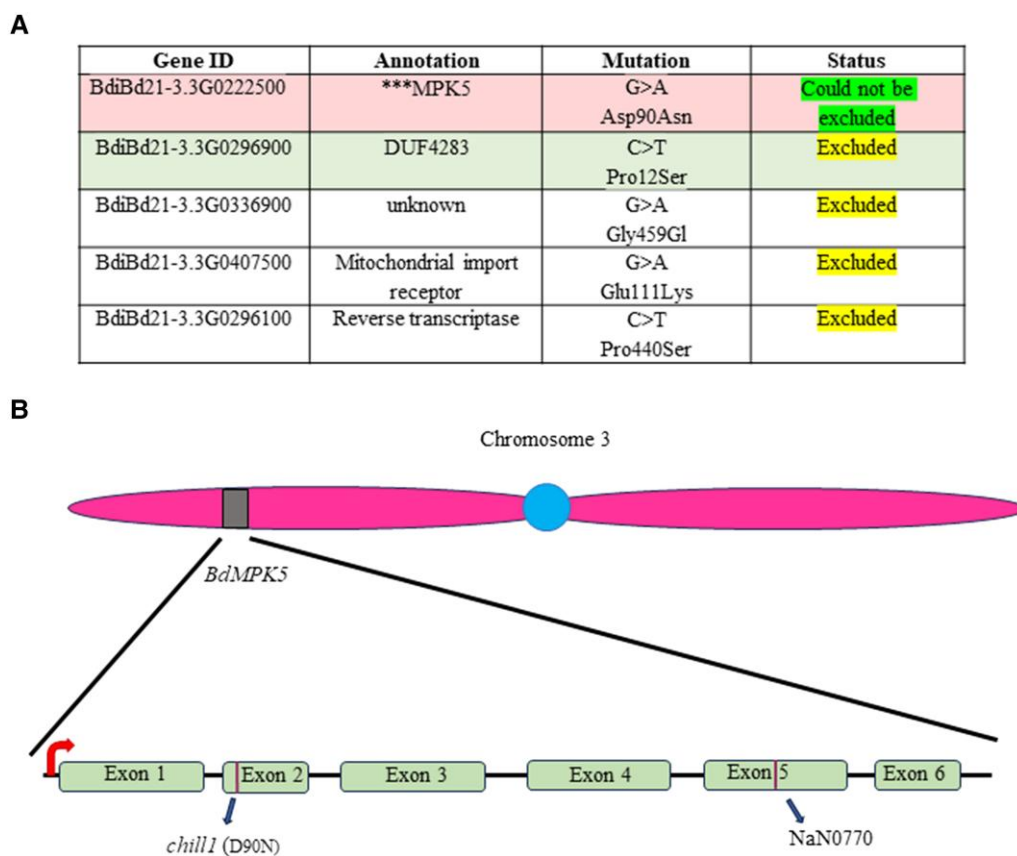
A

Gene ID	Annotation	Mutation	Status
BdiBd21-3.3G0222500	***MPK5	G>A Asp90Asn	Could not be excluded
BdiBd21-3.3G0296900	DUF4283	C>T Pro12Ser	Excluded
BdiBd21-3.3G0336900	unknown	G>A Gly459Gl	Excluded
BdiBd21-3.3G0407500	Mitochondrial import receptor	G>A Glu111Lys	Excluded
BdiBd21-3.3G0296100	Reverse transcriptase	C>T Pro440Ser	Excluded

B

Figure 5. Candidate genes derived from BSA. **A)** Variants in genes called as homozygous via BSA for the SM- and M-pools were compiled to create a list of called homozygous candidate mutations (see Results). Highlighted variants are those that were called as potential candidates in both SM- and M-pools. Results of targeted Sanger sequencing are shown in the right column (see Results). The called homozygous mutation (Mutation column) within the 2nd exon of BdiBd21-3.3G0222500 (MPK5) is shown as confirmed via sequencing. **B)** Drawing showing approximate location of the identified *chill1* variant on chromosome 3 and exon/intron structure on *BdMPK5* showing sites of *chill1* and NaN0770 mutations.

sustained predicted impactful mutations in *BdMPK5* were taken into the following generation. Three independent CRISPR alleles were isolated and confirmed via Sanger Sequencing that included frame shift mutations (Fig. 7B; Supplementary Fig. S5B; CRISPR #1, CRISPR #2, and CRISPR #3).

Stomatal conductance analyses were pursued in T3 generation cas9-less CRISPR plants. Interestingly, CRISPR alleles exhibited a constitutively high stomatal conductance which did not decrease in response to shifts to high CO_2 conditions (800 ppm) (Fig. 8, A and B). Note that in some experiments, *chill1* mutant leaves showed a slight stomatal opening response upon exposure to low CO_2, which may depend on growth conditions (compare Figs. 1D and 8A). However, *chill1* mutant leaves consistently showed a robust impairment in high CO_2-induced stomatal closing under the imposed conditions (e.g. Figs. 1D and 8A). In further stomatal conductance analyses, $2\,\mu M$ ABA was added to the transpiration stream and a strong decline in stomatal conductance was observed in T3 generation CRISPR lines (Fig. 8, C and D, and Supplementary Fig. S6, A and B), showing that CRISPR alleles exhibit a strong CO_2 insensitivity, but functional ABA responses. Genotype-blinded stomatal index and density analyses were pursued for these lines. While the stomatal density for CRISPR #1 was calculated to be significantly different from both the WT control and *chill1*, stomatal density in the CRISPR #2 was not found to be significantly different; and neither line was found to be significantly different from controls when stomatal index was calculated (Fig. 8, E and F). Furthermore, the CRISPR#1 line had a high

stomatal conductance (Fig. 8A), indicating that the observed lower stomatal density did not appreciably affect the overall stomatal conductance of this mutant line.

To further examine whether the *chill1* mutation in *Bdmpk5* is responsible for the *chill1* phenotype, we crossed the *Bdmpk5* CRISPR#2 mutant allele with *chill1* and analyzed F1 plants by infrared imaging and gas exchange analyses. F1 generation plants of the CRISPR#2 allele crossed to the *chill1* mutant showed clear cool leaf canopy phenotypes following exposure of plants to high (1,000 ppm) CO_2, further supporting that the *BdMPK5* variant is responsible for the *chill1* phenotype (Fig. 9A). The CRISPR#2 × *chill1* F1 generation cross was also used in gas exchange analyses and showed very limited response to altered CO_2 similar to the phenotypes observed in both CRISPR #2 and *chill1* mutant lines (Fig. 9B).

Reconstitution of CO_2 sensory function of BdMPK5 and disruption by *chill1* mutation

Blast analysis against *A. thaliana* genes suggested that the mapped BdiBd21-3.3G0222500 (*BdMPK5*) gene encodes the highest *B. distachyon* percentage sequence similarity to the *A. thaliana* AtMPK12 and AtMPK4 proteins (AT2G46070 and AT4G01370) (Supplementary Fig. S4). BdMPK5 has 79% identity to the protein coding sequence of AtMPK12 and 84% identity to AtMPK4. A recent study showed that the *A. thaliana* AtMPK12 and AtMPK4 proteins function as part of the primary CO_2/bicarbonate sensor together with the HT1 protein kinase that mediate CO_2 control of stomatal
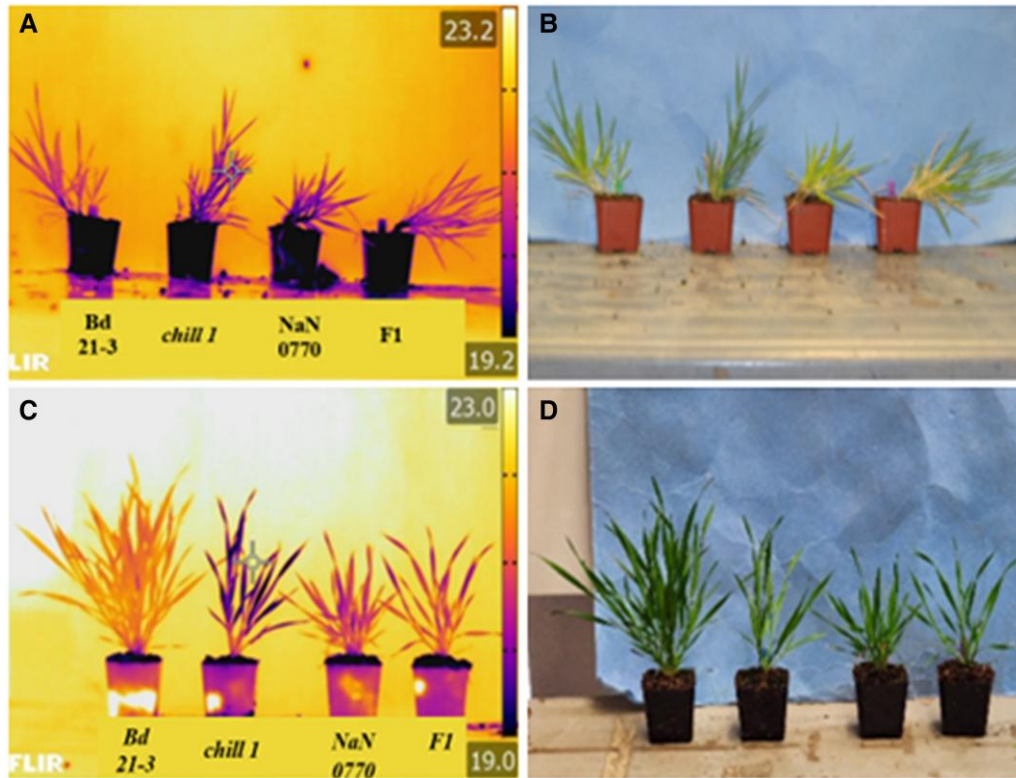
Figure 6. NaN line 0770 crosses. **A)** Four- to 5-wk-old *chill1*, sequence-indexed and confirmed NaN line, and the Bd21-3 × NaN0770 F1 backcross were exposed to 1,000 ppm CO$_2$ for 2 h alongside the Bd21-3 parent (WT) control. **B)** Color images were taken at the same time for identification of plants. Plants from left to right are labeled Bd21-3 (WT), *chill1*, NaN0770, and the F1 NaN0770 backcross. **C)** The NaN-mutagenized NaN0770 line was crossed to *chill1*, and the F1 plants were used for infrared imaging following exposure to high (1,000 ppm) CO$_2$. **D)** Color image of the same plants. Plants from left to right are Bd21-3, *chill1*, NaN0770, and the *chill1* x NaN0770 F1 cross. Pseudo-colored temperature scale is on the right in **A)** and **C)** (°C).
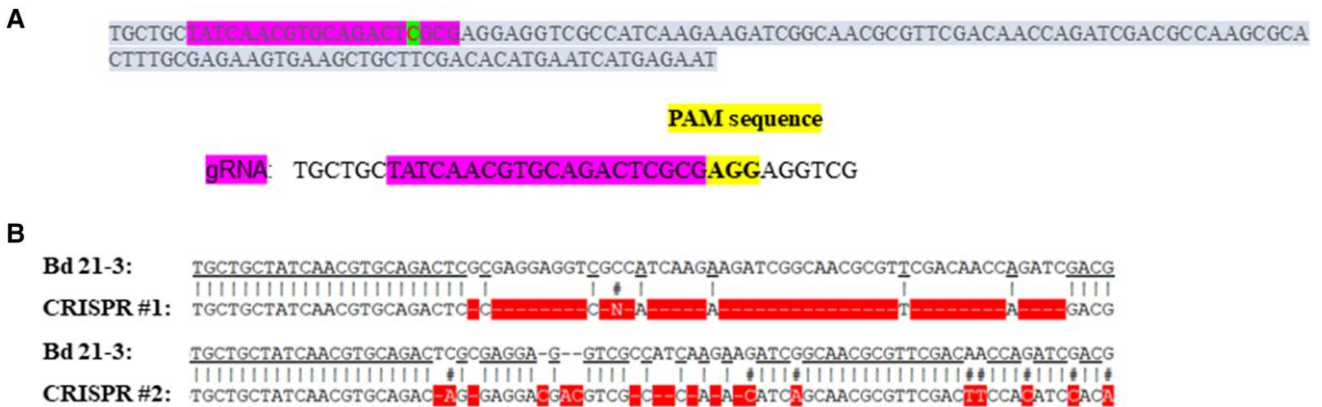

Figure 7. Design for and sequencing of isolated *chill1* CRISPR plants. **A)** gRNA design used in generation of CRISPR plants in the Bd21-3 (WT) parent background (highlighted in pink) and followed by the PAM sequence (highlighted in yellow). Immediately upstream of the PAM sequence is the predicted mutation site (highlighted in green). **B)** Plants generated using this gRNA were sequenced, and 2 of the alleles generated are shown aligned to the parent sequence. Alignment mismatches between the CRISPR alleles and parent line are highlighted in red showing several small deletions near the PAM sequence. # symbols indicate mismatches for which another nucleotide was detected at that locus.

movements (Takahashi et al. 2022). Recent findings showed that HT1 activates the downstream protein kinase CBC1 by phosphorylating CBC1 (Takahashi et al. 2022). Furthermore, this activation of CBC1 is inhibited by elevated CO$_2$/bicarbonate only when HT1, CBC1, and MPK4 or MPK12 are included in the reconstituted reaction (Takahashi et al. 2022). In vitro protein kinase assays were pursued using the recombinant BdMPK5 protein to investigate whether BdMPK5 shows a CO$_2$ response together with HT1 and CBC1. HT1 and CBC1 together with the BdMPK5 protein showed

a high CO$_2$/bicarbonate-induced downregulation of the CBC1 protein kinase activity (Fig. 10A, Supplementary Fig. S7A). The high CO$_2$/bicarbonate response was similar to high CO$_2$ responses found for AtMPK4 and AtMPK12, but not for the clade member AtMPK11 (Takahashi et al. 2022).

We next investigated whether the BdMPK5-D90N variant identified in the *chill1* mutant has an effect on CO$_2$-mediated downregulation of CBC1 phosphorylation. Interestingly, the *chill1* BdMPK5-D90N variant protein abrogated the high
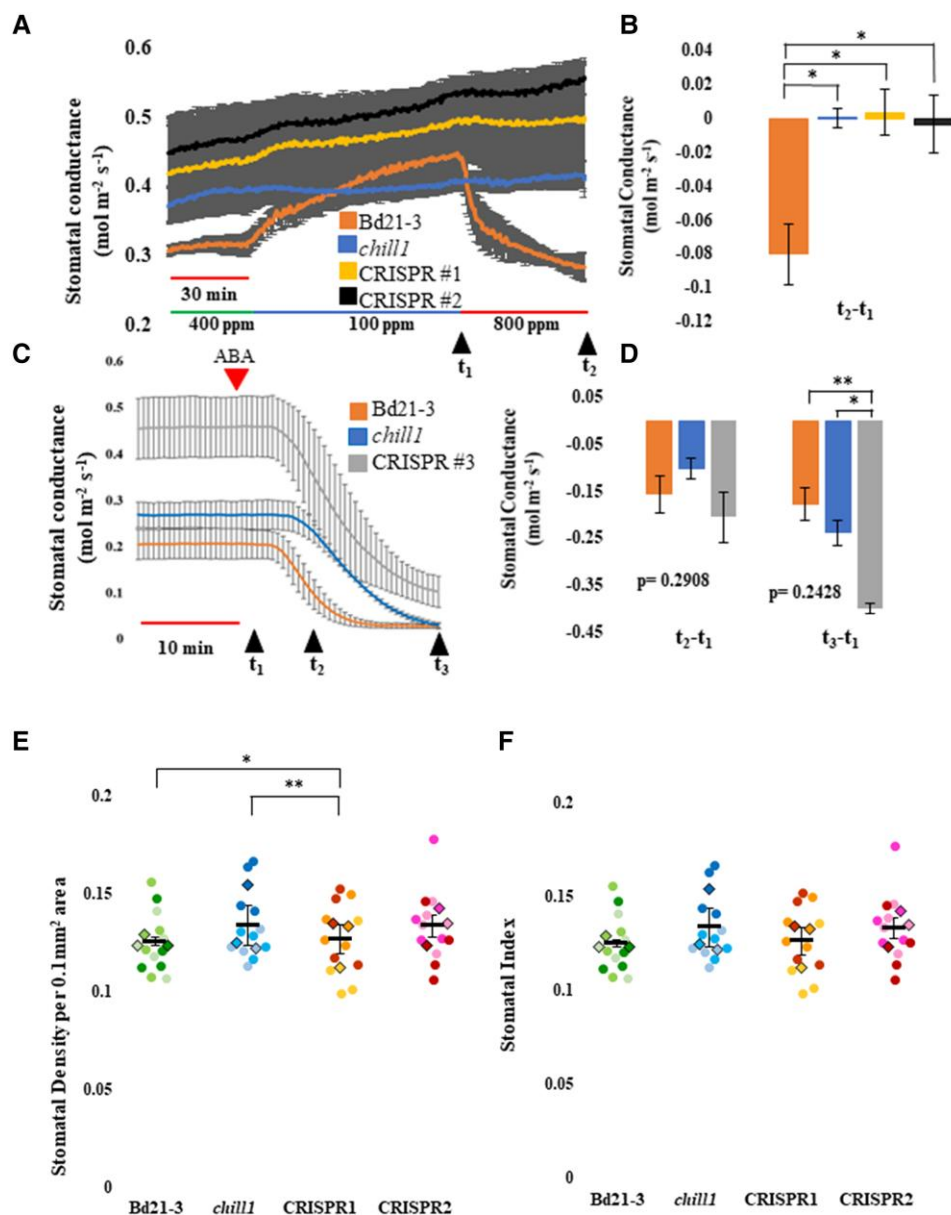
Figure 8. *Bdmpk5* CRISPR alleles show strong CO_2 insensitivity but functional ABA responses. **A, C)** Five- to 6-wk-old plants were analyzed in time-resolved stomatal conductance analyses. **A)** CRISPR alleles show strongly impaired stomatal responses to CO_2 shifts. Data shown are the average of $n = 3 \pm$ SEM experiments using 4 leaves per genotype in each experiment for which the WT control is Bd21-3. **B)** Stomatal conductance changes $\pm$ SEM as calculated at the indicated time points in panel **A)** for $n = 3$ replicates per genotype. Statistical analyses were conducted by 1-way ANOVA with post hoc Tukey tests wherein $t_2 - t_1$ *P*-value < 0.0093. **P*-value < 0.05. Colors correspond to the legend provided in panel **A)**. **C)** CRISPR leaves show functional ABA-induced stomatal closing, despite the large stomatal conductance. Stomatal conductance was recorded for 10 min prior to addition of 2 μM ABA. Data shown are the average of $n = 3 \pm$ SEM experiments using 1 leaf per experiment and genotype. **D)** Stomatal conductance changes as calculated at the indicated time points from data in panel **C)** $\pm$ SEM for $n = 3$ replicates per genotype. Statistical analyses were conducted by 1-way ANOVA with post hoc Tukey tests. **P*-value < 0.05, ***P*-value of <0.01. *P*-values were calculated for the whole data set, comparing WT, *chill1*, and CRISPR lines #3 at the indicated time points. Colors correspond to the legend provided in panel **C)**. **E, F)** Stomatal density **E)** and stomatal index **F)** were determined using leaf imprints created of the 4th true leaf with 3 biological replicates per genotype. Circles represent counts per each image, while diamonds are the average per each of the 3 experiments. Error bars represent SEM, while *P*-values were obtained from 2-tailed *t* tests comparing mutant to the Bd21-3 parent line ("WT"). Data shown are the average of 4 leaves per plant, with 3 independent biological replicates per line ($n = 3 \pm$ SEM). **P*-value < 0.05, ***P*-value of <0.01.

CO_2/bicarbonate-mediated downregulation of CBC1 phosphorylation (Fig. 10A, Supplementary Fig. S7A). These experiments showed that BdMPK5 can replace AtMPK4 and AtMPK12 in the reconstitution of this CO_2 response and that the *chill1* variant in BdMPK5 cannot mediate downstream regulation of CBC1 protein phosphorylation (Fig. 10A).

We further tested the BdMPK5 protein kinase activity. A very weak autophosphorylation activity of the recombinant WT

BdMPK5 protein was detected in the in vitro phosphorylation assays (Fig. 10B; Supplementary Fig. S7B). Surprisingly, introducing the *chill1* mutation showed almost no effect on the BdMPK5 autophosphorylation activity (Fig. 10B; Supplementary Fig. S7B). We introduced point mutations that are predicted to disrupt the protein kinase activity of Chill1 based on homology to other protein kinases. These point mutations in the conserved amino acids in the protein kinase domain (G66R in the glycine-rich loop, K83R
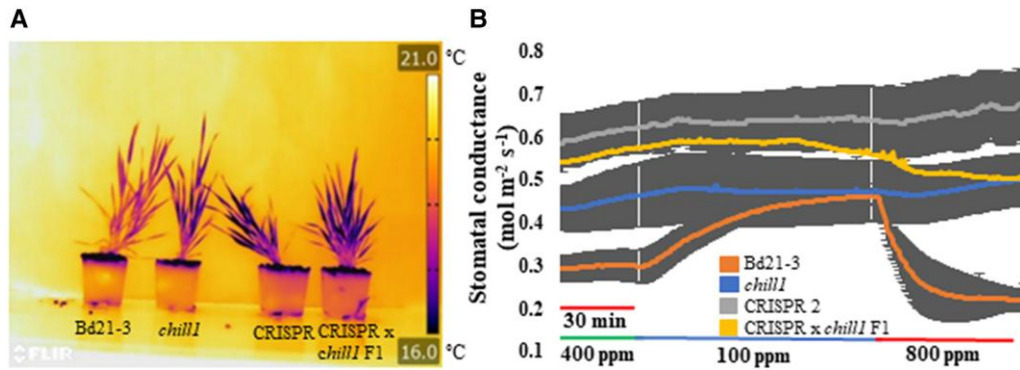
Figure 9. Characterization of CRISPR × *chill1* F1 cross. **A)** The CRISPR#1 *Bdmpk5* mutant was crossed to *chill1*. Five- to 6-wk-old F1 plants were analyzed by infrared imaging following 2 h exposure to high (1,000 ppm) CO$_2$. Plants from left to right are Bd21-3 parent control, *chill1*, CRSPR#1, and *chill1* × CRISPR#1 F1 cross. White vertical lines indicate CO$_2$ concentration transition points. Pseudo-colored temperature scale is on the right in °C. **B)** Stomatal conductance was quantified using a gas exchange analyzer. Data shown are the average of $n = 3$ plants per genotype ± SEM using 4 leaves per plant (12 leaves per genotype), except CRISPR x chill1 F1 cross ($n = 1$ plant & 4 leaves).
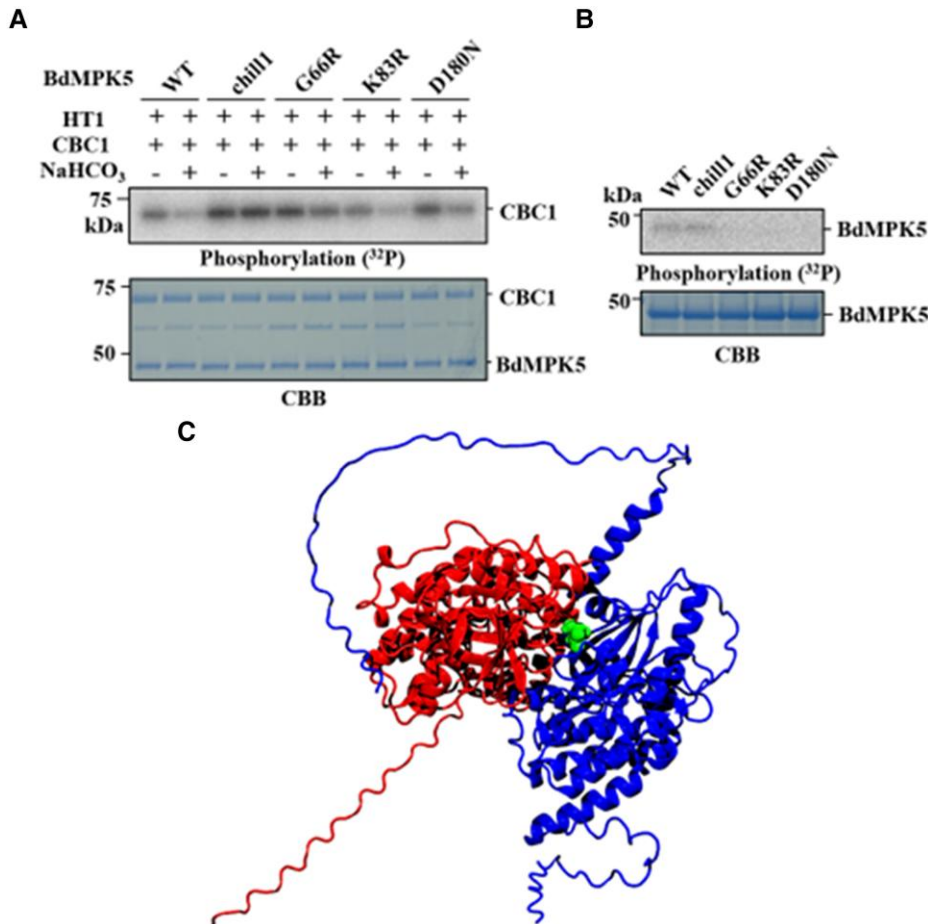

Figure 10. BdMPK5 functions together with *Arabidopsis* HT1 and CBC1 in high CO$_2$/bicarbonate-mediated downregulation of CBC1 protein kinase phosphorylation, protein kinase activity of BdMPK5 and Chill1 isoform, and structural prediction of BdMPK5–BdHT1 complex. **A)** In contrast to WT BdMPK5 protein and the kinase-inactive mutant isoforms BdMPK5-K83R and BdMPK5-D180N, the *chill1* mutant BdMPK5(D90N) variant isoform does not mediate CO$_2$/HCO$_3^-$-dependent downregulation of CBC1 kinase phosphorylation. In vitro phosphorylation assays were performed using GST-CBC1, His-HT1, and His-BdMPK5 (WT, chill1(D90N), G66R, K83R, and D180N) recombinant proteins with (+) or without (−) 20 mM NaHCO$_3$. 20 mM NaCl was added in "-" controls. Phosphorylation levels of CBC1 (top) and Coomassie brilliant blue (CBB)-stained gels (bottom) are shown. **B)** In vitro kinase activity of His-BdMPK5 (WT, chill1(D90N), G66R, K83R, and D180N) recombinant proteins (top) and CBB-stained gel (bottom) are shown (see Results).
C) AlphaFold2-predicted complex of BdMPK5-D90N with BdHT1. BdMPK5 is shown in red, while BdHT1 is shown in blue. The BdMPK5-N90 residue, which is mutant in *chill1*, is colored green (balls at center) and is predicted, based on the BdMPK5-D90N–BdHT1 simulation, to lie at the interface of BdMPK5 and BdHT1.

in the AxK motif (Yeh et al. 2023), and D180N in the catalytic loop) clearly disrupted the BdMPK5 protein kinase activity (Fig. 10B; Supplementary Fig. S7B). Among these kinase-inactive BdMPK5 variants, only the G66R mutation clearly impaired the reconstituted CO_2/HCO_3^- sensing in vitro (Fig. 10A, Supplementary Fig. S7A). These results are consistent with previous unexpected findings that MPK12 kinase activity was not required for CO_2 sensing in *Arabidopsis* (Takahashi et al. 2022).

BdMPK5–BdHT1 structural model predicts that *chill1* mutant residue lies at protein–protein interface

To gain insight into the mechanism by which the BdMPK5-D90N protein disrupts CO_2-induced stomatal closing in planta (Figs. 1 to 3, 8, 9) and reconstitution of a CO_2 sensing core in vitro (Fig. 10A, Supplementary Fig. S7), we pursued AlphaFold2 modeling (Jumper et al. 2021; Evans et al. 2022) to predict the BdMPK5–BdHT1 protein complex structure (Fig. 10C) (see Materials and methods). Interestingly, the mutant residue BdMPK5-D90N is predicted to lie directly at the interaction surface of BdMPK5 and BdHT1 (Fig. 10C).

Discussion

CO_2-regulated stomatal closure can increase WUE in grasses by reducing water loss through transpiration (De Souza et al. 2008; Allen et al. 2011; Wang et al. 2015; Chen et al. 2017). However, to our knowledge, no forward genetic screen of stomatal responses to increased CO_2 in grasses has been reported to date. In the present study, we have developed an unbiased forward genetic screen in the grass *B. distachyon* to identify mutants showing altered canopy leaf temperature under elevated CO_2. Mutant lines were isolated and confirmed throughout 3 individual stages of infrared screening. BSA, resequencing of candidate genes in individual segregating F4 plants, analysis of sequence-indexed Na$^+$-azide mutagenized lines, CRISPR-cas9-generated *bdmpk5* alleles, and CRSPR allele × *chill1* F1 cross analyses further confirmed mapping of the mutant locus *chill1* to the *BdMPK5* gene. CRISPR alleles showed a higher stomatal steady-state conductance than the *chill1* mutant at ambient CO_2 and showed a strong disruption of responsiveness to an increase in the CO_2 concentration. This increased stomatal conductance is likely due to higher impact mutations, including frame shift mutations sustained in the investigated CRISPR lines (Fig. 7B and Supplementary Fig. S5B) as opposed to the *chill1* mutation that has a substitution of a single base and produces a functional recombinant protein (Fig. 10B and Supplementary Fig. S7B). The higher stomatal conductance phenotype in the independent CRISPR lines found here is consistent with strong stomatal conductance phenotypes in mutants that disrupt CO_2 signal transduction (Zhang et al. 2018).

BdMPK5 shows correlation to major component of CO_2/bicarbonate sensor

Although *A. thaliana* is the most widely used eudicot model organism, *B. distachyon* is an emerging model organism for monocots due to the high evolutionary collinearity to important cereal crops such as wheat (International Brachypodium Initiative 2010; Brkljacic et al. 2011, Scholthof et al. 2018). Some components of the CO_2 signaling cascade appear to be conserved across monocots and eudicots such as β-carbonic anhydrases which have been documented to perform similar functions in stomatal CO_2 responses in Arabidopsis, rice, and maize (Hu et al. 2010, 2015;

Chen et al. 2017; Kolbe et al. 2018) and the functions of the SLAC1 anion channel in CO_2 regulation of stomatal conductance in *Arabidopsis* and rice (Negi et al. 2008; Vahisalu et al. 2008; Kusumi et al. 2012). However, stomatal CO_2 sensing mechanisms and the underlying signal transduction pathway remain unknown in grasses. A recent study identified AtMPK4/12 (Des Marais et al. 2014; Jakobson et al 2016; Tõldsepp et al. 2018) and the Raf-like kinase AtHT1 (Hashimoto et al. 2006) as the 2 components that together function as a primary biosensor for stomatal CO_2/bicarbonate signal transduction controlling stomatal movements in Arabidopsis (Takahashi et al. 2022). Our protein sequence analyses show that BdMPK5 has the highest sequence similarity to AtMPK12 and AtMPK4 in *A. thaliana* (Supplementary Fig. S4), further suggesting a level of conservation between CO_2 signaling in both species. While no direct AtMPK4 ortholog was found in *B. distachyon*, the highest AtMPK4 protein sequence similarity was determined to be BdMPK5 (Supplementary Fig. S4). This hypothesis is further supported by findings that BdMPK5 could replace AtMPK4/12 in in vitro reconstitution of the "MPK-HT1-CBC1" CO_2 sensing core (Fig. 10A, Supplementary Fig. S7A). In vitro kinase assays have not resolved a strong protein kinase activity of BdMPK5 (Fig. 10B, Supplementary Fig. S7B). Recent research in *Arabidopsis* has shown that the protein kinase activity of MPK4 and MPK12 is not required for in vitro reconstitution of CO_2 signaling and for in planta complementation of stomatal CO_2 signal transduction (Takahashi et al. 2022; Yeh et al. 2023).

Stomatal movements and increased speed in grasses

Grass stomata are composed of guard cells flanked by lateral subsidiary cells which shrink as turgor increases within guard cells (Raschke and Fellows 1971; Franks and Farquhar. 2007; McAusland et al. 2016; Lawson and Vialet-Chabrand 2019; Nunes et al. 2020). This arrangement has been shown to contribute to the increased speed at which grass stomata are able to respond to stimuli, thereby improving WUE (Franks and Farquhar. 2007; Des Marais et al. 2016; McAusland et al. 2016; Raissig et al. 2017; Lawson and Vialet-Chabrand 2019; Nunes et al. 2020). High CO_2 triggers stomatal closure facilitated by ionic efflux out of guard cells leading to a loss of turgor pressure, while subsidiary cells function in direct opposition and increase ion uptake and turgor pressure (Raschke and Fellows, 1971) assisting in the speed of stomatal responses (Raschke 1972; Franks and Farquhar. 2007; McAusland et al. 2016; Raissig et al. 2017; Lawson and Vialet-Chabrand 2019).

B. distachyon has evolutionary similarity to other monocot model species, including maize, wherein the protein with the highest sequence similarity, ZmMPK12, has been predicted to be expressed in both guard cells and subsidiary cells, based on leaf single cell transcriptomics (Sun et al. 2022). Phylogenetic analyses of genes with the highest sequence similarity to the recently uncovered CO_2 sensing mechanism in *Arabidopsis* were conducted to determine homologs of AtMPK12 and AtMPK4, HT1 and CBC1 and CBC2 in the grasses rice, *B. distachyon* and maize (Supplementary Fig. S8). The same study indicates that transcripts of both of the genes with highest sequence similarity to AtHT1 were expressed in maize guard cells but interestingly were not significantly detected in subsidiary cells (Sun et al. 2022). Furthermore, in an independent recent study, transcriptome RNA-sequencing was performed in *B. distachyon* leaves of the control parent (Bd21-3) and in a subsidiary-less Bdmute (*sid*) mutant (Zhang et al. 2022). *BdMPK5* and *BdHT1* transcripts did not show significantly

differentially expressed levels between WT controls (Bd21-3) and a subsidiary cell-less mutant (sid) lending further support to *BdMPK5* being expressed in guard cells (Zhang et al. 2022), with potential expression in subsidiary cells remaining to be determined. Furthermore, these RNA-seq data sets showed substantially larger reads for the highest related sequence to *CBC1* when compared with *BdMPK5* and *BdHT1*, indicating a high *BdCBC1* expression level in both genotypes (Zhang et al. 2022).

Future protein expression studies of BdMPK5 as well as interaction analyses in *B. distachyon* will determine potential CO$_2$-dependent interactions between BdMPK5 and BdHT1 in guard cells and stomatal subsidiary cells. This gives rise to the questions for future studies (i) whether BdHT1 is present only in *B. distachyon* guard cells or in both guard and subsidiary cell types. (ii) Does BdMPK5 contribute to the CO$_2$ response in both guard cells and subsidiary cells or only in guard cells? (iii) Is the protein kinase activity of BdMPK5 required in planta for stomatal CO$_2$ signal transduction? Additional future studies of the *B. distachyon* homologous proteins to HT1 and CBC1 (Supplementary Fig. S8) will be needed for further definitive investigation of CO$_2$/HCO$_3^-$ sensing mechanisms in *B. distachyon*.

The *chill1* mutant was mapped to a SNP that encodes for a BdMPK5-D90N mutation. Interestingly, AlphaFold2 modeling predicts that this amino acid residue lies at the interface of BdMPK5 and BdHT1 (Fig. 10C), which may contribute to the observed disruption of CO$_2$ signaling. CO$_2$ signaling reconstitution analyses show that the BdMPK5-D90N protein disrupts the ability of BdMPK5 to transmit the high CO$_2$/bicarbonate signal (Fig. 10A) consistent with this prediction. Our protein kinase activity analysis, reconstitution assays, and structural modeling data suggest that the *chill1* D90N mutation may impair the CO$_2$/HCO$_3^-$ sensing function of BdMPK5 but does not clearly impair the protein kinase activity.

Conclusions

In summary, an unbiased forward genetic CO$_2$ response screen in *B. distachyon* was developed here and has led to isolation of stomatal CO$_2$ response *chill* mutants. The *chill1* mutant is strongly impaired in stomatal CO$_2$ responses but shows robust ABA-induced stomatal closure. Mapping of the *chill1* mutant to the *BdMPK5* gene and generation and phenotyping of *BdMPK5* NaN and CRISPR-cas9 mutant alleles together with in vitro reconstitution of the CO$_2$ sensing core with BdMPK5 and structural modeling suggest that *CHILL1* encodes a component of the CO$_2$ sensor in grasses. Future mapping of additional mutants and characterization of BdMPK5 in guard cells and stomatal subsidiary cells provides a powerful system for further dissection of stomatal CO$_2$ sensing and signaling mechanisms in grasses.

Materials and methods
Plant growth conditions

The M5 and subsequent generations of an EMS-mutagenized Brachypodium (*B. distachyon*) seed library obtained from the Joint Genome Institute (JGI) were grown alongside the WT parent control (Bd21-3). All seeds were cold-treated for a minimum of 5 d at 4 °C prior to sowing. Seeds were sown in soil containing a mixture of perlite, vermiculite, and Osmocote following manufacturer's instructions (3:1:1 soil: perlite: vermiculite). Trays were covered with transparent domes which were removed 7 d following emergence of first true leaves. Plants were grown under ambient CO$_2$ concentrations and 16/8 light/dark conditions under 200 to 250 μE m^{-2} s^{-1} light intensity which was found to improve growth conditions, as compared with early experiments with 150 μE m^{-2} s^{-1} light intensities. Sequence-indexed NaN-mutagenized lines were grown under the same conditions alongside appropriate controls and the WT Bd21-3 parent line.

Infrared imaging analyses

Four- to 5-wk-old well-watered *B. distachyon* plants were imaged using an infrared FLIR Imaging camera T650sc (FLIR Systems, Inc. Wilsonville, OR 97070 USA). Ambient CO$_2$ imaging was performed at ~450 ppm CO$_2$ within a plant growth room. Infrared thermal imaging at elevated CO$_2$ was conducted at a minimum of 900 ppm by placing plants within Percival, E-36HO high-CO$_2$ chambers. Imaging was conducted immediately following removal of plants from high-CO$_2$ chambers before plants were able to equilibrate. Plants were removed from the chamber in small, staggered batches and arranged in groups containing WT (Bd21-3) for comparative high-throughput screening. All captured infrared and corresponding parallel photographic images were qualitatively analyzed individually by at least 2 laboratory members to reduce bias. To further reduce selection of false positives in infrared imaging selection for subsequent BSA mapping, F2 plants were compared with parallel-grown WT control plants as well as to each other in an effort to only select those with robust phenotypes.

Stomatal conductance analyses

Healthy 5- to 6-wk-old plants were selected for gas exchange analyses to measure stomatal conductance (gs) using Licor gas exchange analyzers (LI-6800, LI-COR, Lincoln, NE, USA, or LI-6400XT, LI-COR, Lincoln, NE, USA). Prior to analysis, 4 leaves were bound together using micropore tape (3 M), abaxial side downwards as described in Ceciliato et al. (2019). Leaves were allowed to equilibrate within the analyzer for 1 h under ambient CO$_2$ of 400 ppm, 65% humidity, with a light intensity of 250 μmol m^{-2} s^{-1}. Data are representative of average data of 3 experiments each using 4 leaves per experiment (minimum total = 12 leaves per genotype).

Statistical analyses

Statistical ANOVA analyses were conducted using an online ANOVA calculator from astatsa with post hoc Tukey tests (Vasavada 2016). Error bars for graphs are based on SEM as calculated by SD divided by the square root of the number of repeat experiments.

Microscopy

Stomatal imaging was performed by creating an imprint of the 4th true leaf from healthy 5- to 6-wk-old plants. Leaves were glued onto slides using quick-dry super glue to mount the abaxial side to the slide which was then peeled off ~45 min later once the glue was dry. The resulting imprint was imaged via a compound fluorescence microscope and attached camera. A total of 4 images were taken per leaf at 40× magnification with 3 biological replicates per experiment for a total of 12 images per genotype. Stomatal imaging was done by capturing 2 images above the main vein and 2 below to account for uneven dispersal of stomata. Counting of stomata and pavement cells was done using the "cell-counter" function of ImageJ (Schindelin et al. 2012).

Crossing

Crossing *B. distachyon* plants was performed over a 2-d period in 5- to 6-wk-old plants. Individual spikelets containing mature stigma but that had not yet developed mature anthers were used in Day 1, and each spikelet was then emasculated. Flowers were taped at the base of the flower with micropore tape (3 M), and both anthers were removed using fine pointed forceps without damaging stigma or rupturing anthers. All other flowers were removed from the inflorescence following emasculation. The following day, mature anthers were harvested and placed onto a slide inside of a closed plate with a wet paper towel to increase humidity and promote dehiscence. Only anthers that dehisce without manual rupturing are to be used for pollination and were applied to stigma of the emasculated plants from the previous day that did not show any signs of wilting. Plants were then returned to the growth room and kept under well-watered conditions. Seed development should be visible after ~4 d.

Generation of tillers and growth conditions

F1 progeny generated by backcrossing to WT (Bd21-3) were grown under short day (8 h light/16 h dark) to promote large growth of plants and aerial root formation. Once aerial root formation could be observed, tillers were created by using a razor blade to make a cut below the node from which the roots grew (Supplementary Fig. S2). Tillers were immediately placed into Falcon tubes containing a mix of water and 1× fertilizing solution (Technigro, Agawam, MA, USA) and grown under short day conditions (8 h light/16 h dark). After a minimum of 7 d, cuts were transferred to soil and remained covered with domes to maintain increased humidity for ~2 wks (Supplementary Fig. S2). Once plants were established in soil, domes were removed, and light conditions were switched to long day (22 h light/2 h dark) which promotes flowering. F1 tiller populations were allowed to self-cross. F2 seeds were harvested and grown in staggered batches under short day to be used for infrared imaging and subsequent DNA extraction.

F2 selection

Four- to 5-wk-old F2 *chill1* lines backcrossed with the Bd21-3 parent line were analyzed by infrared imaging alongside Bd 21-3 (WT) plants following exposure to 1,000 ppm CO_2 for 2 h. Approximately 560 individual plants were screened, and images were analyzed independently by 3 persons. Plants were sorted based on selections made by laboratory members and were placed into groups to keep only those appearing to have the most robust phenotype. F2 plants selected independently by all 3 persons as showing WT-like canopy temperature formed the "WT-pool" to be used for comparison to plants with *chill1-like* phenotypes for BSA (Michelmore et al. 1991). To reduce selection of false positive chill1-like plants, all images were screened in a very conservative manner by 3 independent lab members. Only plants that were selected to be clearly *chill1*-like by all 3 persons would become the "M" or "mutant" pool. A subset of this pool (SM-pool) selected to be the strongest phenotypically was created by 1 laboratory member by reanalyzing only those plants which had already been designated as *chill1*- like by all 3 persons after individual analyses had been compiled. DNA was extracted from all selected plants using the DNeasy Plant Min Kit (Qiagen, Hilden, Germany), pooled, and sent out for sequencing via Novogene (Davis, CA).

BSA

Sequence data files obtained from Novogene short read WGS were first run through quality checks (Ewing and Green 1998) before proceeding with analysis, and all pools were aligned to a *B. distachyon* reference sequence obtained via Phytozome (https://phytozome-next.jgi.doe.gov/). Sequences were converted from SAM file format to BAM before being sorted and indexed using samtools (Li et al 2009). GATK (Van der Auwera and O'Connor 2020) was then used to mark duplicate sequences, add headers to columns, as well create a BAM index. Before proceeding, the reference genome also needed to be prepared before it could be utilized within GATK. Following this, variants were called using the haplotypecaller function of GATK for both M- and SM-pools and SNPs and indels were separated into 2 separate files for each pool. VariantFiltration was used on all 4 generated files which were then exported using VariantsToTable to be used in QTLseqr. Variants were annotated using snpEff. The R package QTLseqr was used to import SNP data from GATK, verify total read depth, and check reference allele frequency and the SNP-index as well as filter SNPs. QTLseqr was also used for running the QTLseq analysis as well as the G' analysis and generating plots and producing summary tables (Magwene et al 2011; Takagi et al 2013).

Creation of CRISPR lines

CRISPR lines were designed to induce small deletions in BdMPK5 by generating gRNA with the following oligos: Chill1_CRISPR_Fw (ACTTGTATCAACGTGCAGACTCGCG) and Chill1_CRISPR_Rv (AAACCGCGAGTCTGCACGTTGATAC). Oligos were phosphorylated and utilized in a Golden Gate Reaction to be ligated into the CRISPR destination vector JD633 (Addgene). JD633-*chill1* plasmid was used to transform *Escherichia coli* (TOP10) and screened with kanamycin containing media. The destination vector JD633 contains hygromycin resistance as required for transformation by the Boyce Thompson Institute (BTI). Assembled and sequence confirmed plasmids were sent to BTI for transformation in the Bd 21-3 parent background. Lines were screened on plates for hygromycin resistance before shipping. Lines received from BTI were screened again via imaging using the FLIR infrared thermal imaging camera as well as by genotyping to confirm the presence of mutations in the target site. Lines were also genotyped in T2 to confirm the absence of active cas9 to prevent further sustained off target mutations. All sequencing was done via Sanger Sequencing (Retrogen, San Diego, CA).

Phylogenetic analyses

Protein sequence data of the AtHT1 gene were retrieved from Phytozome (https://phytozome-next.jgi.doe.gov/) (Goodstein et al. 2012). For Supplementary Fig. S8, the sequences were used as search queries in Blast searches against the genomes of Brachypodium (https://phytozome-next.jgi.doe.gov/info/Bdistachyon Bd21_3_v1_1), rice (https://phytozome-next.jgi.doe.gov/info/Osativa_v7_0), and maize (https://phytozome-next.jgi.doe.gov/info/Zmays_RefGen_V4). Multiple-sequence alignments and phylogenetic analyses were performed using ClustalOmega software with default settings (https://www.ebi.ac.uk/Tools/msa/clustalo/) (Madeira et al. 2022). The same methodologies were applied to the phylogenetic analysis of BdMPK5, AtMPK4/AtMPK12, and BdCBC1/BdCBC2.

In vitro phosphorylation assays

In vitro phosphorylation assays of WT, Chill1-D90N, and 3 kinase-inactive point mutant isoforms were performed as described previously (Takahashi et al. 2022). In brief, for in vitro CO_2/HCO_3^- sensing assays, 0.5 µg GST-AtCBC1, 0.01 µg His-AtHT1, and 0.5 µg His-BdMPK5 (WT, D90N, G66R, K83R or

D180N) recombinant proteins were incubated in reaction buffer (50 mM Tris-HCl [pH 7.5], 10 mM MgCl2, 0.1% Triton X-100, and 1 mM DTT) with 20 mM $NaHCO_3$ or 20 mM NaCl (control) for 30 min, and then, phosphorylation reactions were carried out for 30 min with 200 μM ATP and 1 μCi [γ-32P]-ATP. For BdMPK5 protein kinase activity assays, 5 μg recombinant His-BdMPK5 proteins were incubated with 1 μCi ^{32}P-ATP and 200 μM cold ATP for 30 min.

Structural predictions of BdMPK5–BdHT1

The BdMPK5–BdHT1 complex structure was predicted with AlphaFold2, version 2.3.2 using the multimer functionality (Jumper et al. 2021; Evans et al. 2022). The source code was downloaded from the AlphaFold2 GitHub page (https://github.com/deepmind/alphafold). The sequences of BdMPK5-D90N and BdHT1 were used for structure predictions. We predicted the complex of BdHT1 (BdiBd21-3.1G0477700) (NCBI protein ID: XP_003563578) with BdMPK5 (BdiBd21-3.3G0222500). The maximum template release date we used was "January 1, 3000". The Triton Shared Computing Cluster (SDSC 2022) at the San Diego Supercomputer Center was used for modeling BdMPK5–BdHT1 structures. We used the full genetic database configuration and included a final relaxation step on all predicted models. For complex prediction, we created 5 BdMPK5–BdHT1 complex models (e.g. Takahashi et al. 2022), each starting with a random seed, and, for each of these models, made 5 structure predictions. We then ranked all 25 predictions and used the top ranked prediction as our final model. This ranking system uses the predicted template modeling (pTM) score, which may produce a different set of rankings than if one uses the predicted local difference distance test (pLDDT) score to rank structures. However, apart from the manually set maximum template release date, all of these settings were the default ones provided by AlphaFold2. This workflow was similar to previous predictions of MPK–HT1 complexes (Takahashi et al. 2022).

Accession numbers

Sequence data from this article can be found in the GenBank/ EMBL data libraries under accession numbers AtMPK4 (AT4G01370), AtMPK12 (AT2G46070), AtHT1 (AT1G62400), BdMPK5 (BdiBd21-3.3G0222500), and AtMPK11 (AT1G01560).

Acknowledgments

Author contributions

Supplementary data

Funding

Data availability

The author responsible for distribution of materials integral to the findings presented in this article in accordance with the policy described in the Instructions for Authors is the corresponding last author.

References

Allen LH, Kakani VG, Vu JCV, Boote KJ. Elevated CO_2 increases water use efficiency by sustaining photosynthesis of water-limited maize and sorghum. *J Plant Physiol.* 2011:168(16):1909–1918. https://doi.org/10.1016/j.jplph.2011.05.005

Asseng S, Ewert F, Martre P, Rötter RP, Lobell DB, Cammarano D, Kimball BA, Ottman MJ, Wall GW, White JW, *et al.* Rising temperatures reduce global wheat production. *Nature Climate Change, [online].* 2015:5(2):143–147. https://doi.org/10.1038/nclimate2470

Bertolino LT, Caine RS, Gray JE. Impact of stomatal density and morphology on water-use efficiency in a changing world. *Front Plant Sci*. 2019:10:225. https://doi.org/10.3389/fpls.2019.00225

Brkljacic J, Grotewold E, Scholl R, Mockler T, Garvin DF, Vain P, Brutnell T, Sibout R, Bevan M, Budak H, et al. Brachypodium as a model for the grasses: today and the future. *Plant Physiol*. 2011:157(1):3–13. https://doi.org/10.1104/pp.111.179531

Ceciliato PHO, Zhang J, Liu Q, Shen X, Hu H, Liu C, Schäffner AR, Schroeder JI. Intact leaf gas exchange provides a robust method for measuring the kinetics of stomatal conductance responses to abscisic acid and other small molecules in Arabidopsis and grasses. *Plant Methods*. 2019:15(1):38. https://doi.org/10.1186/s13007-019-0423-y

Chen T, Wu H, Wu J, Fan X, Li X, Lin Y. Absence of OsβCA1 causes a CO_2 deficit and affects leaf photosynthesis and the stomatal response to CO_2 in rice. *Plant J*. 2017:90(2):344–357. https://doi.org/10.1111/tpj.13497

Cingolani P, Platts A, Wang LL, Coon M, Nguyen T, Wang L, Land SJ, Lu X, Ruden DM. A program for annotating and predicting the effects of single nucleotide polymorphisms, SnpEff: SNPs in the genome of Drosophila melanogaster strain w1118; iso-2; iso-3. *Fly (Austin)*. 2012:6(2):80–92. https://doi.org/10.4161/fly.19695

Dalmais M, Antelme S, Ho-Yue-Kuang S, Wang Y, Darracq O, d'Yvoire MB, Cézard L, Légée F, Blondet E, Oria N, et al. A TILLING platform for functional genomics in Brachypodium distachyon. *PLoS One* 2013:8(6):e65503–e65503. https://doi.org/10.1371/journal.pone.0065503

Des Marais DL, Auchincloss LC, Sukamtoh E, McKay JK, Logan T, Richards JH, Juenger TE. Variation in MPK12 affects water use efficiency in Arabidopsis and reveals a pleiotropic link between guard cell size and ABA response. *Proc Natl Acad Sci U S A*. 2014:111(7):2836–2841. https://doi.org/10.1073/pnas.1321429111

Evans R, O'Neill M, Pritzel A, Antropova N, Senior A, Green T, Žídek A, Bates R, Blackwell S, Yim J, et al. Protein complex prediction with AlphaFold-multimer. bioRxiv 463034. https://doi.org/10.1101/2021.10.04.463034, 10 March 2022, preprint: not peer reviewed.

Ewing B, Green P. Base-calling of automated sequencer traces usingphred.II. Error probabilities. *Genome Res*. 1998:8(3):186–194. https://doi.org/10.1101/gr.8.3.186

Fahad S, Bajwa AA, Nazir U, Anjum SA, Farooq A, Zohaib A, Sadia S, Nasim W, Adkins S, Saud S, et al. Crop production under drought and heat stress: plant responses and management options. *Front Plant Sci*. 2017:8:1147. https://doi.org/10.3389/fpls.2017.01147

Franks PJ, Farquhar GD. The mechanical diversity of stomata and its significance in gas-exchange control. *Plant Physiol*. 2007:143(1):78–87. https://doi.org/10.1104/pp.106.089367

Goodstein DM, Shu S, Howson R, Neupane R, Hayes RD, Fazo J, Mitros T, Dirks W, Hellsten U, Putnam N, et al. Phytozome: a comparative platform for green plant genomics. *Nucleic Acids Res*. 2012:40(D1):D1178–D1186. https://doi.org/10.1093/nar/gkr944

Harrison EL, Arce Cubas L, Gray JE, Hepworth C. The influence of stomatal morphology and distribution on photosynthetic gas exchange. *Plant J*. 2020:101(4):768–779. https://doi.org/10.1111/tpj.14560

Hashimoto M, Negi J, Young J, Israelsson M, Schroeder JI, Iba K. Arabidopsis HT1 kinase controls stomatal movements in response to CO_2. *Nat Cell Biol*. 2006:8(4):391–397. https://doi.org/10.1038/ncb1387

Hauser F, Ceciliato PHO, Lin YC, Guo D, Gregerson JD, Abbasi N, Youhanna D, Park J, Dubeaux G, Shani E, et al. A seed resource for screening functionally redundant genes and isolation of new mutants impaired in CO_2 and ABA responses. *J Exp Bot*. 2019:70(2):641–651. https://doi.org/10.1093/jxb/ery363

Hetherington AM, Woodward FI. The role of stomata in sensing and driving environmental change. *Nature* 2003:424(6951):901–908. https://doi.org/10.1038/nature01843

Hiyama A, Takemiya A, Munemasa S, Okuma E, Sugiyama N, Tada Y, Murata Y, Shimazaki K. Blue light and CO_2 signals converge to regulate light-induced stomatal opening. *Nat Commun*. 2017:8(1):1284. https://doi.org/10.1038/s41467-017-01237-5

Hu H, Boisson-Dernier A, Israelsson-Nordström M, Böhmer M, Xue S, Ries A, Godoski J, Kuhn JM, Schroeder JI. Carbonic anhydrases are upstream regulators of CO2-controlled stomatal movements in guard cells. *Nat Cell Biol*. 2010:12(1):87–93. https://doi.org/10.1038/ncb2009

Hu H, Rappel W-J, Occhipinti R, Ries A, Böhmer M, You L, Xiao C, Engineer CB, Boron WF, Schroeder JI. Distinct cellular locations of carbonic anhydrases mediate carbon dioxide control of stomatal movements. *Plant Physiol*. 2015:169(2):1168–1178. https://doi.org/10.1104/pp.15.00646

International Brachypodium Initiative. Genome sequencing and analysis of the model grass *Brachypodium distachyon*. *Nature* 2010:463(7282):763–768. https://doi.org/10.1038/nature08747

Jakobson L, Vaahtera L, Tõldsepp K, Nuhkat M, Wang C, Wang Y-S, Hõrak H, Valk E, Pechter P, Sindarovska Y, et al. Natural variation in Arabidopsis Cvi-0 accession reveals an important role of MPK12 in guard cell CO_2 signaling. *PLoS Biol*. 2016:14(12):e2000322. https://doi.org/10.1371/journal.pbio.2000322

Jumper J, Evans R, Pritzel A, Green T, Figurnov M, Ronneberger O, Tunyasuvunakool K, Bates R, Žídek A, Potapenko A, et al. Highly accurate protein structure prediction with AlphaFold. *Nature* 2021:596-(7873):583–589. https://doi.org/10.1038/s41586-021-03819-2

Keller B, Feuillet C. Colinearity and gene density in grass genomes. *Trends Plant Sci*. 2000:5(6):246–251. https://doi.org/10.1016/s1360-1385(00)01629-0

Kolbe AR, Brutnell TP, Cousins AB, Studer AJ. Carbonic anhydrase mutants in *Zea mays* have altered stomatal responses to environmental signals. *Plant Physiol*. 2018:177(3):980–989. https://doi.org/10.1104/pp.18.00176

Kusumi K, Hirotsuka S, Kumamaru T, Iba K. Increased leaf photosynthesis caused by elevated stomatal conductance in a rice mutant deficient in SLAC1, a guard cell anion channel protein. *J Exp Bot*. 2012:63(15):5635–5644. https://doi.org/10.1093/jxb/ers216

Lawson T, Vialet-Chabrand S. Speedy stomata, photosynthesis and plant water use efficiency. *New Phytol*. 2019:221(1):93–98. https://doi.org/10.1111/nph.15330

Li H, Handsaker B, Wysoker A, Fennell T, Ruan J, Homer N, Marth G, Abecasis G, Durbin R. The sequence alignment/map format and SAMtools. *Bioinformatics*. 2009:25(16):2078–2079. https://doi.org/10.1093/bioinformatics/btp352

MacRobbie EAC. ABA activates multiple Ca2+ fluxes in stomatal guard cells, triggering vacuolar K+(Rb+) release. *Proc Natl Acad Sci U S A*. 2000:97(22):12361–12368. https://doi.org/10.1073/pnas.220417197

MacRobbie EAC. Control of volume and turgor in stomatal guard cells. *J Membr Biol*. 2006:210(2):131–142. https://doi.org/10.1007/s00232-005-0851-7

Madeira F, Pearce M, Tivey ARN, Basutkar P, Lee J, Edbali O, Madhusoodanan N, Kolesnikov A, Lopez R. Search and sequence analysis tools services from EMBL-EBI in 2022. *Nucleic Acids Res*. 2022:50(W1):W276–W279. https://doi.org/10.1093/nar/gkac240

Magwene PM, Willis JH, Kelly JK. The statistics of bulk segregant analysis using next generation sequencing. *PLoS Comput Biol*. 2011:7-(11):e1002255. https://doi.org/10.1371/journal.pcbi.1002255

Mansfeld BN, Grumet R. QTLseqr: an R package for bulk segregant analysis with next-generation sequencing. *Plant Genome*. 2018:11(2):0. https://doi.org/10.3835/plantgenome2018.01.0006

Marais DLD, Razzaque S, Hernandez KM, Garvin DF, Juenger ET. Quantitative trait loci associated with natural diversity in water-use efficiency and response to soil drying in *Brachypodium distachyon*. *Plant Sci*. 2016:251:2–11. https://doi.org/10.1016/j.plantsci.2016.03.010

Marten H, Hyun T, Gomi K, Seo S, Hedrich R, Roelfsema MRG. Silencing ofNtMPK4 impairs CO2-induced stomatal closure, activation of anion channels and cytosolic Ca2+signals in *Nicotiana tabacum* guard cells. *Plant J*. 2008:55(4):698–708. https://doi.org/10.1111/j.1365-313x.2008.03542.x

McAusland L, Vialet-Chabrand S, Davey P, Baker NR, Brendel O, Lawson T. Effects of kinetics of light-induced stomatal responses on photosynthesis and water-use efficiency. *New Phytol*. 2016:211(4):1209–1220. https://doi.org/10.1111/nph.14000

Merlot S, Mustilli A-C, Genty B, North H, Lefebvre V, Sotta B, Vavasseur A, Giraudat J. Use of infrared thermal imaging to isolate Arabidopsis mutants defective in stomatal regulation. *Plant J*. 2002:30(5): 601–609. https://doi.org/10.1046/j.1365-313x.2002.01322.x

Michelmore RW, Paran I, Kesseli RV. Identification of markers linked to disease-resistance genes by bulked segregant analysis: a rapid method to detect markers in specific genomic regions by using segregating populations. *Proc Natl Acad Sci U S A*. 1991:88(21): 9828–9832. https://doi.org/10.1073/pnas.88.21.9828

Mustilli A-C. Arabidopsis OST1 protein kinase mediates the regulation of stomatal aperture by abscisic acid and acts upstream of reactive oxygen species production. *Plant Cell*. 2002:14(12): 3089–3099. https://doi.org/10.1105/tpc.007906

NASA Graphic. The relentless rise of carbon dioxide. 2022. [accessed 2023 Nov 16]. https://climate.nasa.gov/climate_resources/24/graphic-the-relentless-rise-of-carbon-dioxide/.

Negi J, Matsuda O, Nagasawa T, Oba Y, Takahashi H, Kawai-Yamada M, Uchimiya H, Hashimoto M, Iba K. CO$_2$ regulator SLAC1 and its homologues are essential for anion homeostasis in plant cells. *Nature* 2008:452(7186):483–486. https://doi.org/10.1038/nature06720

Nunes TDG, Zhang D, Raissig MT. Form, development and function of grass stomata. *Plant J*. 2020:101(4):780–799. https://doi.org/10.1111/tpj.14552

O'Connor DL, Elton S, Ticchiarelli F, Hsia MM, Vogel JP, Leyser O. Cross-species functional diversity within the PIN auxin efflux protein family. *eLife* 2017:6:e31804. https://doi.org/10.7554/elife.31804

Phytozome. Brachypodium distachyon Bd21-3 v1.1 DOE-JGI. [accessed 2023 Jul 13]. https://phytozome-next.jgi.doe.gov/.

Raissig MT, Matos JL, Anleu Gil MX, Kornfeld A, Bettadapur A, Abrash E, Allison HR, Badgley G, Vogel JP, Berry JA, *et al*. Mobile MUTE specifies subsidiary cells to build physiologically improved grass stomata. *Science* 2017:355(6330):1215–1218. https://doi.org/10.1126/science.aal3254

Raissig MT, Woods DP. The wild grass *Brachypodium distachyon* as a developmental model system. *Curr Top Dev Biol*. 2022:147:33–71. https://doi.org/10.1016/bs.ctdb.2021.12.012

Raschke K. Saturation kinetics of the velocity of stomatal closing in response to CO$_2$. *Plant Physiol*. 1972:49(2):229–234. https://doi.org/10.1104/pp.49.2.229

Raschke K. Stomatal action. *An Rev Plant Physiol*. 1975:26(1):309–340. https://doi.org/10.1146/annurev.pp.26.060175.001521

Raschke K, Fellows MP. Stomatal movement in *Zea mays*: shuttle of potassium and chloride between guard cells and subsidiary cells. *Planta* 1971:101(4):296–316. https://doi.org/10.1007/bf00398116

Schindelin J, Arganda-Carreras I, Frise E, Kaynig V, Longair M, Pietzsch T, Preibisch S, Rueden C, Saalfeld S, Schmid B, *et al*. Fiji: an open-source platform for biological-image analysis. *Nat methods*. 2012:9(7):676–682. https://doi.org/10.1038/nmeth.2019

Scholthof K-BG, Irigoyen S, Catalan P, Mandadi KK. Brachypodium: a monocot grass model genus for plant biology. *Plant Cell*. 2018:30(8):1673–1694. https://doi.org/10.1105/tpc.18.00083

SDSC: San Diego Supercomputer Center. Triton shared computing cluster. University of California, San Diego. Service 2022. https://doi.org/10.57873/T34W2R

Sherrard ME, Maherali H. The adaptive significance of drought escape in *Avena barbata*, an annual grass. *Evolution* 2006:60(12):2478–2489. https://doi.org/10.1111/j.0014-3820.2006.tb01883.x

Souza DPA, Gaspar M, Silva EAD, Ulian EC, Waclawovsky AJ, Nishiyama MY Jr, Santos RVD, Teixeira MM, Souza GM, Buckeridge MS. Elevated CO$_2$ increases photosynthesis, biomass and productivity, and modifies gene expression in sugarcane. *Plant Cell Environ*. 2008:31(8):1116–1127. https://doi.org/10.1111/j.1365-3040.2008.01822.x

Stocker TF, Qin D, Plattner G-K, Tignor M, Allen SK, Boschung J, Nauels A, Xia Y, Bex V, Midgley PM, editors. IPCC, 2013: climate change 2013: the physical science basis. *Contribution of working group I to the fifth assessment report of the intergovernmental panel on climate change*. Cambridge, United Kingdom and New York (NY), USA: Cambridge University Press; 2013. p. 1535.

Sun G, Xia M, Li J, Ma W, Li Q, Xie J, Bai S, Fang S, Sun T, Feng X, *et al*. The maize single-nucleus transcriptome comprehensively describes signaling networks governing movement and development of grass stomata. *Plant Cell*. 2022:34(5):1890–1911. https://doi.org/10.1093/plcell/koac047

Takagi H, Abe A, Yoshida K, Kosugi S, Natsume S, Mitsuoka C, Uemura A, Utsushi H, Tamiru M, Takuno S, *et al*. QTL-seq: rapid mapping of quantitative trait loci in rice by whole genome resequencing of DNA from two bulked populations. *Plant J*. 2013:74(1):174–183. https://doi.org/10.1111/tpj.12105

Takahashi Y, Bosmans KC, Hsu P-K, Paul K, Seitz C, Yeh C-Y, Wang Y-S, Yarmolinsky D, Sierla M, Vahisalu T, *et al*. Stomatal CO$_2$/bicarbonate sensor consists of two interacting protein kinases, Raf-like HT1 and non-kinase-activity activity requiring MPK12/MPK4. *Sci Adv*. 2022:8(49):eabq6161. https://doi.org/10.1126/sciadv.abq6161

Tõldsepp K, Zhang J, Takahashi Y, Sindarovska Y, Hõrak H, Ceciliato PHO, Koolmeister K, Wang Y-S, Vaahtera L, Jakobson L, *et al*. Mitogen-activated protein kinases MPK4 and MPK12 are key components mediating CO2 -induced stomatal movements. *Plant J* 2018:96(5):1018–1035. https://doi.org/10.1111/tpj.14087

Vahisalu T, Kollist H, Wang Y-F, Nishimura N, Chan W-Y, Valerio G, Lamminmäki A, Brosché M, Moldau H, Desikan R, *et al*. SLAC1 is required for plant guard cell S-type anion channel function in stomatal signalling. *Nature* 2008:452(7186):487–491. https://doi.org/10.1038/nature06608

Van der Auwera GA, O'Connor BD. *Genomics in the cloud: using Docker, GATK, and WDL in Terra*. 1st edn. Sebastopol, California: O'Reilly Media; 2020.

Vasavada N. ANOVA with post-hoc Tukey HSD test calculator with Scheffé, Bonferroni and Holm multiple comparison—input k, the number of treatments. [online] Astatsa.com. 2016. [accessed 2024 Mar 5]. https://astatsa.com/OneWay_Anova_with_TukeyHSD/

Vogel J, Bragg J. *Brachypodium distachyon*, a new model for the *Triticeae*. In: Feuillet C, Muehlbauer GJ, editors. *Genetics and genomics of the Triticeae*. New York, NY: Springer; 2009. p. 427–449.

Wahid A, Gelani S, Ashraf M, Foolad M. Heat tolerance in plants: an overview. *Environ Exp Bot*. 2007:61(3):199–223. https://doi.org/10.1016/j.envexpbot.2007.05.011

Wang M, Xie B, Fu Y, Dong C, Hui L, Guanghui L, Liu H. Effects of different elevated CO2 concentrations on chlorophyll contents,

gas exchange, water use efficiency, and PSII activity on C3 and C4 cereal crops in a closed artificial ecosystem. *Photosynth Res*. 2015:126(2–3):351–362. https://doi.org/10.1007/s11120-015-0134-9

Willmer C, Fricker M. The distribution of stomata. *Stomata*. Dordrecht, Netherlands: Springer, Dordrecht; 1996. p. 12–35. https://doi.org/10.1007/978-94-011-0579-8_2

Woods DP, Amasino RM. Dissecting the control of flowering time in grasses using *Brachypodium distachyon*. *Plant genetics and genomics: crops and models*. Cham, Switzerland: Springer; 2015. p. 259–273.

Xie X, Wang Y, Williamson L, Holroyd GH, Tagliavia C, Murchie E, Theobald J, Knight MR, Davies WJ, Leyser HMO, *et al*. The identification of genes involved in the stomatal response to reduced atmospheric relative humidity. *Curr Biol*. 2006:16(9):882–887. https://doi.org/10.1016/j.cub.2006.03.028

Yeh C-Y, Wang Y-S, Takahashi Y, Kuusk K, Paul K, Arjus T, Yadlos O, Schroeder JI, Ilves I, García-Sosa AT, *et al*. MPK12 in stomatal CO_2 signaling: function beyond its kinase activity. *New Phytol*. 2023:239(1):146–158. https://doi.org/10.1111/nph.18913

Zhang D, Spiegelhalder RP, Abrash EB, Nunes TDG, Hidalgo I, Gil MXA, Jesenofsky B, Lindner H, Bergmann DC, Raissig MT. Opposite polarity programs regulate asymmetric subsidiary cell divisions in grasses. *eLife* 2022:11:e79913. https://doi.org/10.7554/elife.79913

Zhang J, De-Oliveira-Ceciliato P, Takahashi Y, Schulze S, Dubeaux G, Hauser F, Azoulay-Shemer T, Tõldsepp K, Kollist H, Rappel W-J, *et al*. Insights into the molecular mechanisms of CO_2-mediated regulation of stomatal movements. *Curr Biol*. 2018:28(23):R1356–R1363. https://doi.org/10.1016/j.cub.2018.10.015

Zheng Y, Li F, Hao L, Yu J, Guo L, Zhou H, Ma C, Zhang X, Xu M. Elevated CO_2 concentration induces photosynthetic downregulation with changes in leaf structure, non-structural carbohydrates and nitrogen content of soybean. *BMC Plant Biol*. 2019:19(1):255. https://doi.org/10.1186/s12870-019-1788-9

Zhu Z, Piao S, Myneni RB, Z, Canadell JG, Ciais P, Sitch S, Friedlingstein P, Arneth A, *et al*. Greening of the earth and its drivers. *Nat Clim Change*. 2016:6(8):791–795. https://doi.org/10.1038/nclimate3004